Ore Geology Reviews 177 (2025) 106450

Contents lists available at ScienceDirect

Ore Geology Reviews

journal homepage: www.elsevier.com/locate/oregeorev

Study on the thermal persistence of silver acetate: Implication for the role of organic acids in metallic mineralization

Zhiyong Ni [a,b], Yanjing Chen [c,*], Kai Shi [a], Haifei Zheng [c]

[a] State Key Laboratory of Petroleum Resources and Engineering, China University of Petroleum, Beijing 102249, China
[b] College of Geosciences, China University of Petroleum, Beijing 102249, China
[c] Key Laboratory of Orogen and Crustal Evolution, Peking University, Beijing 100871, China

ARTICLE INFO

Keywords:
Silver acetate
Hydrothermal diamond anvil cell
Thermal persistence
Thermodynamic modelling
Hydrothermal mineralization

ABSTRACT

Interaction between organic and inorganic fluids can facilitate formation of mineral deposits. Organic acids are common in oilfield brines, and their decomposition can generate H_2O, CO_2 and CH_4 that are abundant in fluid inclusions from hydrothermal mineral deposits. However, little research has been performed on the interaction between organic acid-bearing solution and metals. This study insights into the role of organic acids in metal transportation by examining the thermal persistence of silver acetate at high temperatures and pressures using a hydrothermal diamond anvil cell. The experimental results indicate that silver acetate becomes more persistent at higher pressure at the same temperature. The presence of pyrite facilitates the decomposition of silver acetate at temperatures of 150–330 °C under geothermal gradient of 25 °C/km. Our thermodynamic modeling results also show that organic matter could generate silver acetate and acetic acid at high temperature and pressure, furthermore, silver acetate remain stable and maintain higher concentrations under a lower geothermal gradient with temperatures below 500 °C and pressure above 500 MPa. These observations accord with the geologic fact that large-scale orogenic-type mineralization of Ag, Au and Cu generally occurred in the post-orogenic thermal extension. They also consist with the numerous observations of $CO_2 - H_2O$ inclusions, the carbonate and hydroxylic alterations in the orogenic-type mineral deposits, and the widespread presence of pyrite formed during earlier mineralization stages. This research provides new understanding of organic–inorganic interaction during hydrothermal mineralization, orogeny and thermal evolution of sedimentary basins.

1. Introduction

In some cases, oil accumulations and hydrothermal mineral deposits coexist at both macroscopic and microscopic scales, because they can result from similar geologic processes that involve the formation and migration of hydrothermal fluids and the enrichment of metallic commodities in mineral deposits (Chen et al., 2001; Giordano, 1994; Kesler et al., 1994). Complex interactions between organic and inorganic substances in fluids have been identified during the evolution of sedimentary basins and often linked to the formation of mineral deposits (Broadbent et al., 1998; Etminan and Hoffmann, 1989; Jaraula et al., 2015; Mossman, 1999). Previous works have focused on either the ability of organic fluids (e.g., oil, natural gas, or oilfield brine) to carry metals or the role of organic substances to facilitate metallic precipitation from the fluids during mineral deposit formation (Anderson, 2008; Kesler et al., 1994; Sanz-Robinson and Williams-Jones, 2019; Sun and Püttmann, 2000). It is acknowledged that organic substances can act as reductants or as sulfur sources to form ore minerals such as sulfides, resulting in metal precipitation through processes such as thermochemical sulfate reduction (Anderson, 2015). However, little is known about the direct involvement of organic compounds in metal migration and precipitation processes.

Natural systems, particularly orogenic-type deposits, provide critical contexts for these processes. Orogenic-type deposits are among the most widespread and economically significant mineral systems, often forming during compressional tectonic settings where metamorphic and magmatic fluids interact with organic-rich sedimentary rocks. These deposits frequently contain pyrite, arsenopyrite, and native gold or silver, underscoring the role of sulfur-rich fluids and reductants in ore formation (Chen et al., 2004; Goldfarb et al., 2005; Groves et al., 2020). Organic compounds within these settings are believed to influence the transport and deposition of metals by forming metal–organic complexes

* Corresponding author.
E-mail address: yjchen@pku.edu.cn (Y. Chen).

https://doi.org/10.1016/j.oregeorev.2025.106450
Received 26 September 2024; Received in revised form 28 November 2024; Accepted 7 January 2025
Available online 8 January 2025

or by driving redox reactions that precipitate ore minerals (Ding et al., 2024; Ni et al., 2020). Furthermore, hydrocarbon inclusions and organic acids are often found in quartz veins associated with orogenic systems, linking hydrothermal fluids to organic sources within sedimentary basins (Reith and McPhail, 2006; Sun, 1998). These examples highlight the importance of understanding the interaction between organic and inorganic fluids in natural mineralizing systems.

Previous research investigated the ability of humic acids to bond metals at low temperatures (Baker, 1978; Giordano, 1994), though these findings may not be applicable to high-temperature hydrothermal systems because humic acids are unstable under such conditions (Boles et al., 1988). As an initial product of the thermal evolution of sedimentary organic matter, humus further evolves into organic acids (Tissot and Welte, 2013), including acetic, propionic, butyric, malonic, succinic, and other organic acids, which are common and rich in oilfield brines (up to 10^4 mg/L; Bell et al., 1994; Fisher, 1987; Kharaka et al., 1987). Organic acids and their associated decomposition products (e.g., H_2O and CO_2) are often present in fluid inclusions within hydrothermal mineral deposits (Chen et al., 2022; Drummond and Palmer, 1986; Palmer and Drummond, 1986). The mutual conversion between CO_2 and organic matter is common in both nature and human activity, as exemplified by photosynthesis and fossil fuel combustion (Jin et al., 2011; Jin et al., 2012; Michiels et al., 2015; Zhong et al., 2019; He et al., 2019; Horita and Berndt, 1999). Organic acids, acid anions, and metalorganic complexes are involved in many geological processes across various environment such as the atmosphere, soil, seawater, sedimentary basins, and hydrothermal system (Shock, 1995). At low-temperature, the organic acid anions in solution present in metal-organic complexes decompose more slowly than those present alone as anions (Fein et al. 1995; Nakano et al., 2016), and play an important role in transporting metals to form mineral deposits (Sanz-Robinson and Williams-Jones, 2019; Tu, 1998). However, it remains unclear whether metal–organic compounds are persistent under high temperatures and pressures, and thus capable of transporting metals as precursors to the carbonic fluid inclusions observed in hydrothermal mineral deposits.

This study investigates the thermal persistence of silver acetate under high temperature and pressure using a hydrothermal diamond anvil cell (HDAC). Additional experiments were conducted with pyrite, given its catalytic effect on acetate decomposition (Bell et al., 1994) and its prevalence in hydrothermal deposits, including orogenic-type system. Thermodynamic modeling based on advances in theoretical geochemistry (Helgeson, 1992; Sverjensky et al., 1997; Shock and Koretsky, 1993; Ding et al., 2024) was used to evaluate organic-fluid interactions. The findings highlight the potential of silver acetate in metal transport under extreme conditions and provide new insights into organic–inorganic interactions during the geological evolution of sedimentary basins and orogenic system.

2. High temperature and pressure experiments

2.1. Hydrothermal diamond anvil cell equipment and experimental setup

Experiments were undertaken in a hydrothermal diamond anvil cell (HDAC; Bassett et al., 1993). Samples were loaded into the experimental space—a 0.3 mm diameter hole within a 0.35 mm thick rhenium gasket—by enclosing the gasket with two 0.8 mm diameter diamond anvil faces. To avoid reaction between fluid and Re gaskets, the hole of Re gasket was coated with gold line. Experimental temperatures were determined using a K-type thermocouple and calibrated using the melting points of phenolphthalein (261.5 °C) and stearic acid (69.6 °C) prior to each experimental run (Fig. 1). All experimental temperatures were corrected by this calibration, yielding experimental uncertainties of ±5 °C. Experimental pressures were determined using the Raman shift of quartz (about 464 cm^{-1}). This approach used a quartz chip that

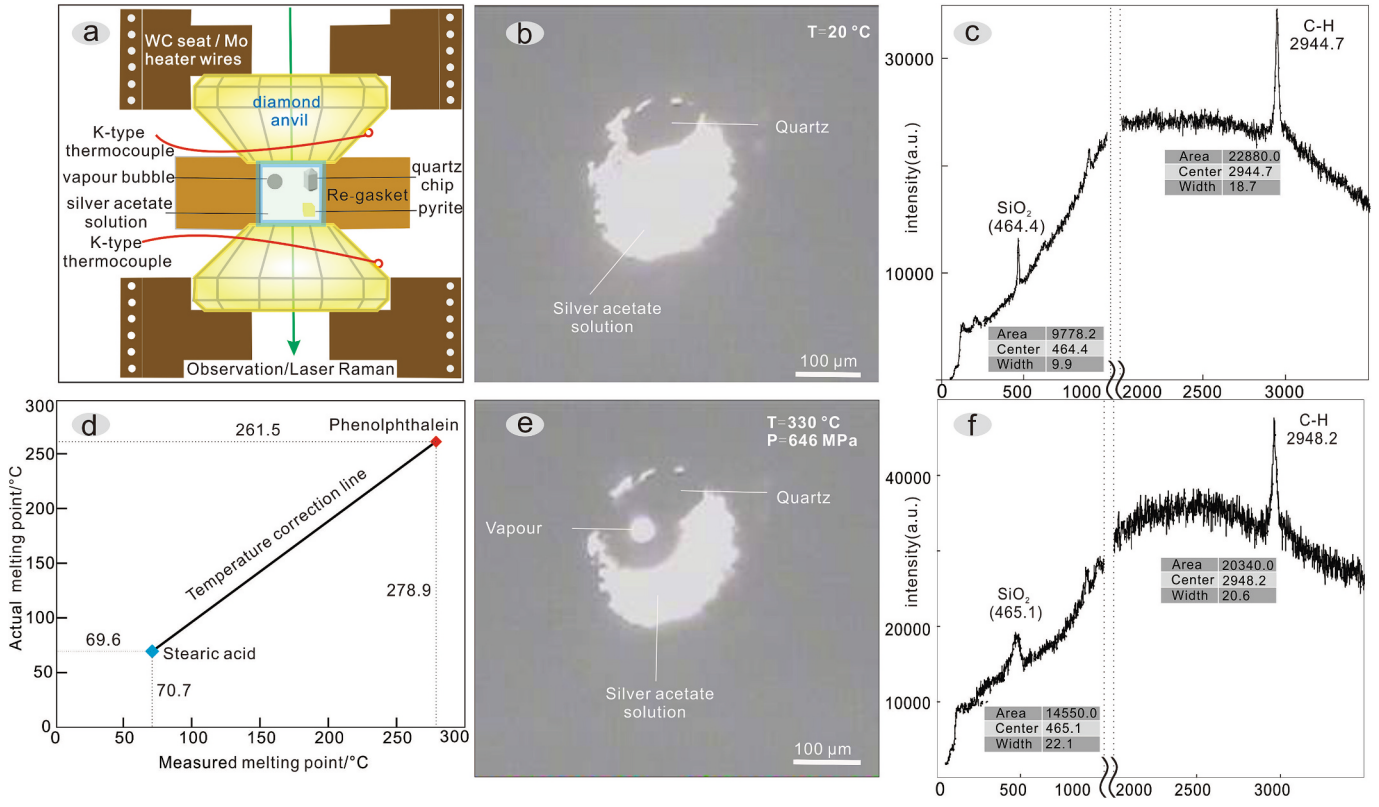

Fig. 1. a. the sketch map of Hydrothermal Diamond Anvil Cell; b and e. state of silver acetate solution at room temperature and high temperature and high pressure (330 °C, 646 MPa); c and f. Raman shift of quartz and C-H symmetric stretching vibration at room temperature and 330 °C, 646 MPa (Area: peak area; Center: the center of peak; Width: full width at half maximum); d. temperature correction of HDAC based on melting point of stearic acid and phenolphthalein.

was placed in the center of the microscope crosshairs during Raman spectroscopy to calibrate the initial Raman shift of the quartz. The pressure within the HDAC was then calculated using the relationship between the shift of the quartz Raman spectrum peak and pressure, with an uncertainty of approximately ±50 MPa (Cui, et al., 2020; Schmidt and Ziemann, 2000; Yuan et al., 2016). This calculation used the following steps: (i) Measuring the Raman shift of the quartz pressure sensor at room temperature and pressure, yielding a measured Raman position of quartz ($\upsilon_{measured,\ T\ =\ 20°C,\ P\ =\ 0.1\ MPa}$) for our experiments. (ii) The calibrated Raman positions (ν_{corr}) of quartz were calculated from Raman band value ($\nu_{measured}$) using the following relationship:

$$\nu_{corr}\ \left(cm^{-1}\right) = \nu_{measured}\ -\ \nu_{l} + \nu_{l,\ standard}$$

where $\nu_{measured}$ denotes the measured Raman position of quartz, and ν_{l} is the position of lamp fluorescence collected after each quartz spectra, and $\nu_{l,\ standard}$ is that of lamp fluorescence that was collected at the beginning of each run of HDAC experiment.

(iii) Calculation of the temperature contribution to ($\Delta\nu_T$) (cm^{-1}) based on ($\Delta\nu_T$) (cm^{-1}) $= 2.50136{\cdot}10^{-11}{\cdot}T^4 + 1.46454{\cdot}10^{-8}{\cdot}T^3 - 1.801{\cdot}10^{-5}{\cdot}T^2 - 0.01216{\cdot}T + 0.29$. (iv) Calibration of the Raman shift of the quartz pressure sensor at different temperatures and pressures ($\nu_{T,\ P}$) and calculating the resulting frequency shift ($\Delta\nu$) caused by pressure as follows: ($\Delta\nu$) (cm^{-1}) $= \nu_{T,\ P} - \nu_{corr} - (\Delta\nu_T)$. (v) Calculation of pressure values (P) in MPa using $0.036079{\cdot}[(\Delta\nu)]^2 + 110.86\ (\Delta\nu)$ ($T < 100\ °C$); P (MPa) $= (\Delta\nu)/0.009 + 0.1$ ($T > 100\ °C$).

At high temperature ($T > 150\ °C$), when the fluorescence is too strong to record Raman shift of the quartz pressure sensor, we use the equation of state (EOS) of NaCl–H_2O with equal molality to CH_3COOAg–H_2O (0.06 mol/l; Pressure < 300 MPa; Brown and Lamb, 1989) and EOS of H_2O to calculate the pressure of the system (Pressure > 300 MPa; Holloway, 1981).

2.2. Reagent preparation

Analytical grade solid silver acetate and deionized water were used as starting materials and for the preparation of silver acetate-saturated solutions. Gem-grade quartz was milled in a mortar to ~100 μm grain size and ore-grade pyrite was crushed to a similar ~100 μm grain size. One of single grain of cube-shaped pyrites with ~100 μm side length was added to silver acetate in CH_3COOAg–FeS_2–H_2O systems. The chemical composition of pyrite is determined by scanning electron microscope with energy dispersive spectrometer (Fig. 2). The diamond anvil, gasket, quartz, and pyrite were cleaned separately in deionized water in an ultrasonic bath for 20 min before being dried on a hotplate to remove any surface contamination.

2.3. Raman spectra measurement and processing

Laser Raman spectroscopy was undertaken in the Laser Raman spectroscopy laboratory of the School of Earth and Space Sciences, Peking University, Beijing, China. Analyses used a HORIBA Jobin Yvon confocal LabRAM HR Evolution laser Raman spectrometer employing a frequency doubled Nd:YAG green laser light source with a wavelength of 532.06 nm. The analyses used a power of 100 nW, a confocal hole width of 500 μm, and scanning wave numbers that ranged from 100 to 4000 cm^{-1}. The resultant data were processed using the SYSTAT Software Inc. Peakfit 4.0 package. The peaks of silver acetate, quartz and fluorescent lamp were all fitted with Pearson IV amplify functions because of the asymmetric properties of those peaks (Yuan et al., 2016).

2.4. Scanning electron microscopic observation

The quenched samples were collected after the HDAC experiment and coated with gold. The samples were observed and compositionally analyzed using the Phenom XL benchtop scanning electron microscope with energy dispersive spectrometer (SEM-EDS) with an accelerating potential of 15 kV at the China University of Petroleum, Beijing.

2.5. Silica capillary tubing experiment equipment

Silver acetate solution (10 g/L) was loaded using round cross-section fused silica capillary tubing with 0.5 mm of inner diameter and 1.5 mm of outer diameter (Polymicro Technologies, U.S.A.). The polyimide coating of the tubing was burned off, and the tubing was cleaned with deionized water before sample loading. The procedures of sealing the capillary tubes were described in detail by Chou et al. (2008). The gas was passively drawn via open split into the IRMS (Trace GC-ISOLINK-MAT 253) for subsequent carbon isotope analysis. The final carbon isotope values represent the average of multiple replicate analyses (generally, n > 2) with a standard deviation of better than 0.2 ‰. All final values are reported relative to the international standard, Vienna Pee Dee Belemnite (VPDB) carbonate.

2.6. Experimental details

Our experiments were divided into two groups, both of which were carried out in closed systems using the HDAC. The first group of experiments started with a solution of 10 g/L silver acetate with densities in the system altered by changing the sizes of the bubbles in the initial sample. Each experimental run was started at room temperature (20 °C) and heated slowly (5 °C/min) to obtain the decomposition temperature of silver acetate under different pressure conditions (Table 1). We

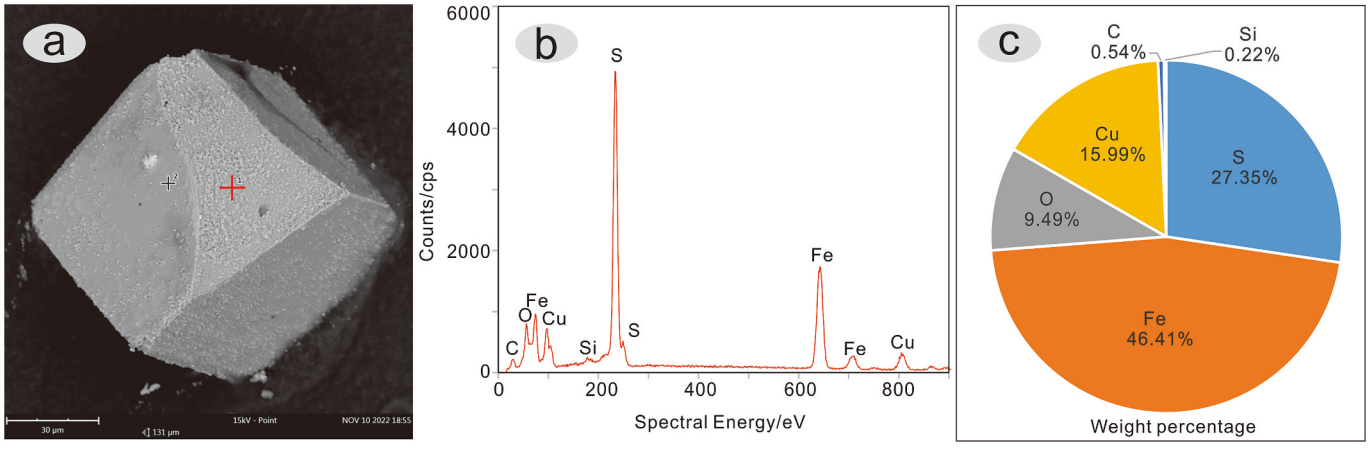

Fig. 2. The chemical composition of pyrite used in the experiments. a. SEM photo of the pyrite; b. EDS results of the pyrite; c. Elemental weight percentage of the pyrite.

Table 1
The decomposition temperature (T) and pressure (P) of silver acetate solution with or without pyrite. (The pressure marked with * and ** are calculated using the equations of state (EOS) of NaCl–H_2 O and H_2 O, respectively).

No.	Homogeneous T (°C)	Decomposition T (°C)	Decomposition P (MPa)	ν_{464} (cm^{-1})
Without pyrite				
Exp. 1–1	93	150	164	464.0
Exp. 1–2	85	165	144*	–
Exp. 1–3	90	178	158*	–
Exp. 1–4	129	221	162*	–
Exp. 1–5	141	244	180*	–
Exp. 1–6	106	313	434**	–
Exp. 1–7	95	322	490**	–
Exp. 1–8	50	330	646**	465.1
With pyrite				
Exp. 2–1	95	103	93	464.1
Exp. 2–2	115	121	102	463.9
Exp. 2–3	127	142	205	464.5
Exp. 2–4	145	156	197*	–
Exp. 2–5	150	162	214*	–
Exp. 2–6	160	173	231*	–
Exp. 2–7	181	198	301*	–
Exp. 2–8	73	236	335**	–
Exp. 2–9	20	250	478**	–
Exp. 2–10	60	330	618**	–

determined the state of the system by microscopy and measured the C–H bond symmetric stretching vibration peak of silver acetate (2945 cm^{-1}) by laser Raman spectroscopy until the experimental system underwent significant changes such as bubbles suddenly appearing or the field of view suddenly blackening. The temperature and the Raman shift of quartz were recorded at this time. The second group of experiments involved the addition of solid pyrite to the 10 g/L silver acetate solution. The heating rate was again controlled at <5 °C/min until obvious changes were observed within the experiment, when the temperature and quartz sensor Raman shift were recorded. The solid decomposition products of silver acetate during this study are determined by SEM-EDS. The gas decomposition products of silver acetate are determined by isotope ratio mass spectrometer (IRMS) with the following steps: (i) The fused silica capillary tubing with 0.5 mm of inner diameter containing silver acetate solution (10 g/L) was heated at 300 °C for 96 h to ensure the decomposition of silver acetate. (ii) The silica capillary tubing was then coated with tinfoil and put into a sealed vessel connecting with vacuum pump. (iii) The sealed vessel was is pumped to near a vacuum state (P < 5 KPa), and the silica capillary tubing in the vessel was crushed to release gas. (iv) The gas was extracted using a 100 μL microinjection needle and injected into the IRMS instrument (Fig. 3). (v) The IRMS experiment result showed that the CO_2 signal (289.3 s retention time) appeared, and the intensity of the extracting gas is significantly higher than that of the air, and the carbon isotopic values ($\delta^{13}C_{PDB}$) of the extracting gas are lower than those of the air (Fig. 3), which suggest that the CO_2 is produced by the decomposition of silver acetate.

3. Results

The thermal persistence of silver acetate at high temperatures and pressures and the ability of this compound to transport metals is investigated using CH_3COOAg–H_2O and CH_3COOAg–FeS_2–H_2O systems employing HDAC (Fig. 1; Bassett et al., 1993).

3.1. Thermal persistence of silver acetate solution

The first group of experiments were designed to investigate the thermal persistence of silver acetate solution (10 g/L). The experiment results indicate that the silver acetate solution is more persistent at higher pressures compared to lower pressures, and its decomposition temperature gradually increases with rising pressure (Fig. 4; Table 1). At pressure of 144 MPa, the decomposition of silver acetate solution occurs at 165 °C and is characterized by the appearance of CO_2 bubbles (Fig. 3, 4a, b). At 434 MPa, the vapor bubble appears when the temperature rises to 313 °C (Fig. 4c, d). At 614 MPa, vapor bubble cannot appear when the temperature rises to 300 °C, even though the reaction time prolongs to 48 h and 96 h (Fig. 4e – h). Despite of this, native silver precipitates from the solution, and more silver precipitates after longer reaction time (Fig. 4f, h), indicating that the decomposition of silver acetate solution is a time-dependent kinetic process.

The solid and vapor generated form silver acetate decomposition during the experiments are identified via scanning electron microscope with energy dispersive spectrometer (SEM-EDS) and isotope ratio mass spectrometer (IRMS), respectively (Figs. 3, 4). The solid generated from silver acetate decomposition is native Ag, and the amount of Ag at high pressure is less than at low pressure (Fig. 4). The gas generated from silver acetate decomposition is CO_2 that is identified by IRMS (Fig. 3), deciphering the transformation mechanism between the organic and CO_2-bearing fluids. The decomposition reaction of silver acetate solution is inferred as below:

$$8\ CH_3COOAg\ (aq) + 2\ H_2O = 8\ Ag\ (\text{native silver}) + 2\ CO_2\ (g) + 7\ CH_3COOH\ (aq) \quad (1)$$

3.2. Pyrite impact on the thermal persistence of silver acetate solution

The second group of experiments were conducted for 10 g/L silver acetate solutions with addition of pyrite crystal. Ten runs of experiments

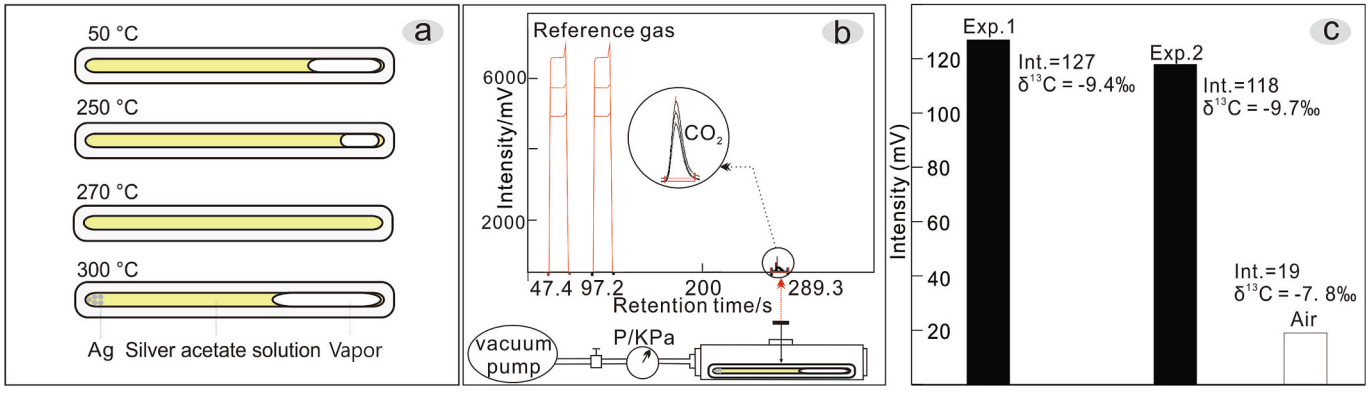

Fig. 3. The gas products of decomposition of silver acetate solution. a. the sketch map silica capillary tubing experiment equipment; b. the sketch map of sealed vessel connecting with vacuum pump and the carbon isotope mass spectrum of extracting gas from silica capillary tubing. c. the intensity of carbon isotope mass spectrum and the carbon isotope value ($\delta C^{13}{}_{PDB}$) of samples and air.

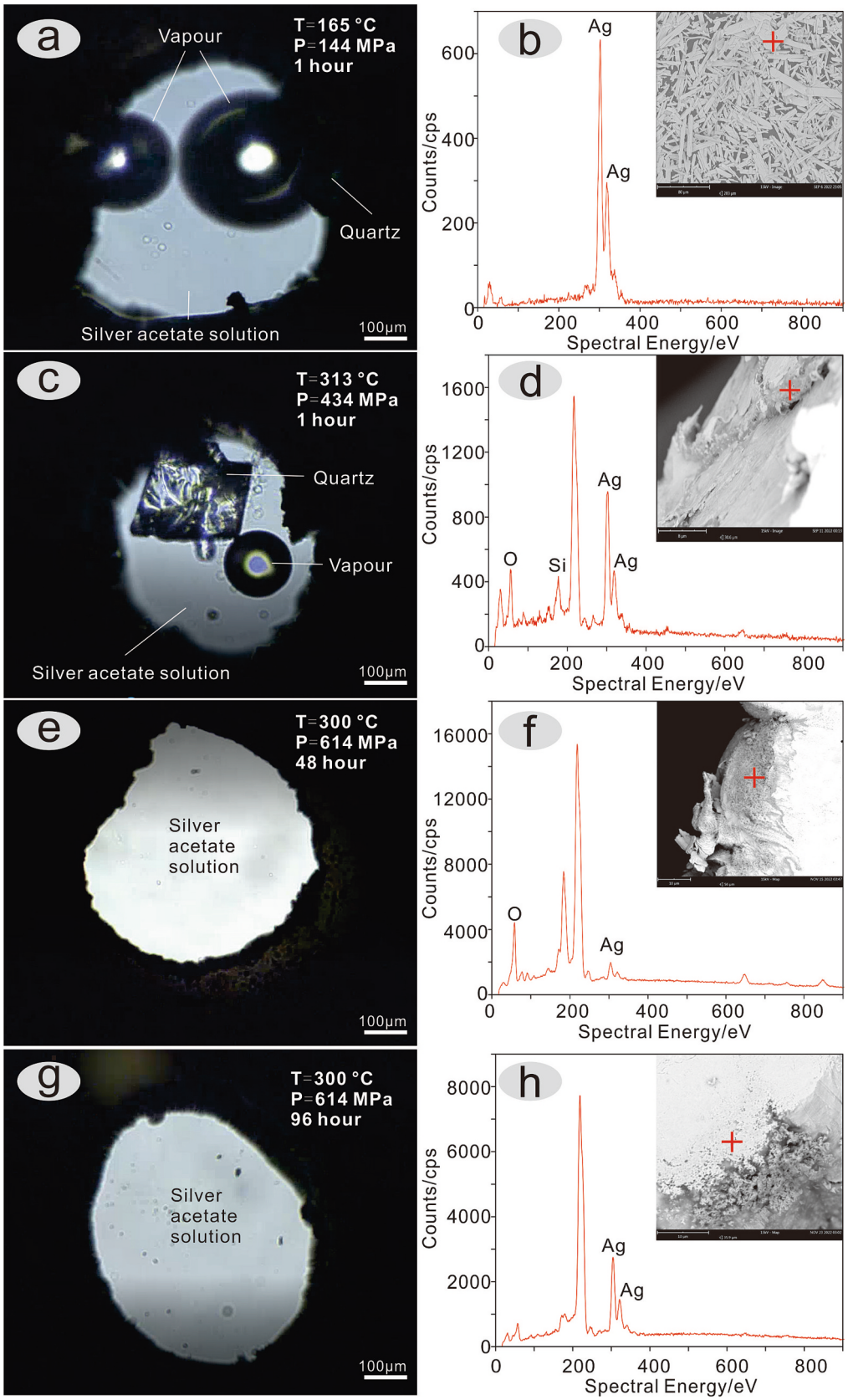

(caption on next page)

Fig. 4. State of silver acetate solution in HDAC at different temperature and pressure. a. At the temperature of 165 °C and the pressure of 144 MPa during 1 h, the decomposition of silver acetate solution is characterized by vapour suddenly appearing (photomicrograph); b. SEM-EDS results show that the diamond anvil face is covered with native silver at the end of experiment; c. At the temperature of 313 °C and the pressure of 434 MPa during 1 h, the decomposition of silver acetate solution is characterized by vapour suddenly appearing (photomicrograph); d. SEM-EDS results show that there exists native silver in the inner wall of the hole of rhenium gasket at the end of experiment; e. Photomicrograph of silver acetate solution at the temperature of 300 °C and the pressure of 614 MPa during 48 h. f. SEM-EDS results show that there exists small amount of native silver in the inner wall of the hole of rhenium gasket at the end of experiment; g. Photomicrograph of silver acetate solution at the temperature of 300 °C and the pressure of 614 MPa during 96 h. h. SEM-EDS results show that there exists more native silver in the inner wall of the hole of rhenium gasket comparing with the experiment during 48 h.

indicate that the presence of pyrite significantly reduces the decomposition temperature of silver acetate compared with the temperatures from pyrite-free experiments at the same or similar pressure (Table 1; Fig. 5). The decomposition reaction is more intense, which is indicated by the appearance of multiple vapor bubbles (Fig. 5). The solid products generated from silver acetate decomposition are native silver, which is proven by the SEM-EDS detection. After the reaction, the solution shows stronger fluorescence intensity and the peak of SO_4^{2-} on the laser Raman spectra (Fig. 5), suggesting that a few pyrite is oxidized during the decomposition of silver acetate solution. The reaction is inferred as below:

$$14\ CH_3COOAg\ (aq) + 6\ H_2O + FeS_2\ (s) = 14\ Ag\ (\text{native silver}) + 2\ CO_2\ (g) + 13\ CH_3COOH + FeSO_4\ (aq) + H_2S\ (g) \quad (2)$$

4. Thermodynamic simulation

It is important to note that our experimental data were based on simple silver acetate solutions. The effects of natural silicate rock assemblages under high-temperature and high-pressure conditions remain to be determined. To investigate these compositional influences, we performed thermodynamic simulation over a wide high P-T range, incorporating organic matter coexisting with carbonaceous mudstone. These simulations were conducted using the HCh software package developed by Shvarov and Bastrakov (2008). The tool effectively determines the compositions of coexisting aqueous fluids and stable mineral assemblages using a free-energy minimization approach, applicable across a temperature range of 0–1000 °C and pressure range of 0–500 MPa. We simulated the water–rock reaction process between organic-rich carbonaceous shales and low-salinity fluids (5 wt% NaCl), which are typical components of the host rocks in sediment-hosted silver deposits and are representative of metamorphic fluids (Goldfarb et al., 2005). To enhance the simulation of silver acetate within silicate mineral assemblages, as well as to investigate the release of silver and the decomposition of organic matter, we examined systems containing elements Ag, Al, C, Ca, Cl, Fe, H, K, Na, O, Si and Ti. The simulations covered a pressure–temperature range of 50–500 °C and 80–500 MPa, corresponding to depths of 5–20 km. The thermodynamic data u for these systems were sourced from Zhong et al. (2015) and Ryzhenko et al. (2016). Carbonaceous shales are s common component of the host rocks in the sediment-hosted silver deposits. For this study, carbonaceous shales from Weishancheng Au-Ag ore belt in central China was used as the starting rock for the model. Their bulk composition is as follows (in wt.%): SiO_2 = 83.8, Al_2O_3 = 5.8, FeO = 2.4, Fe_2O_3 = 2.0, K_2O = 1.9, CaO = 0.6, TiO_2 = 0.3 (Chu et al., 2000). In addition, minor native silver was included in the initial composition, as carbonaceous rocks often contain small amounts of silver, with traces of silver typically found in

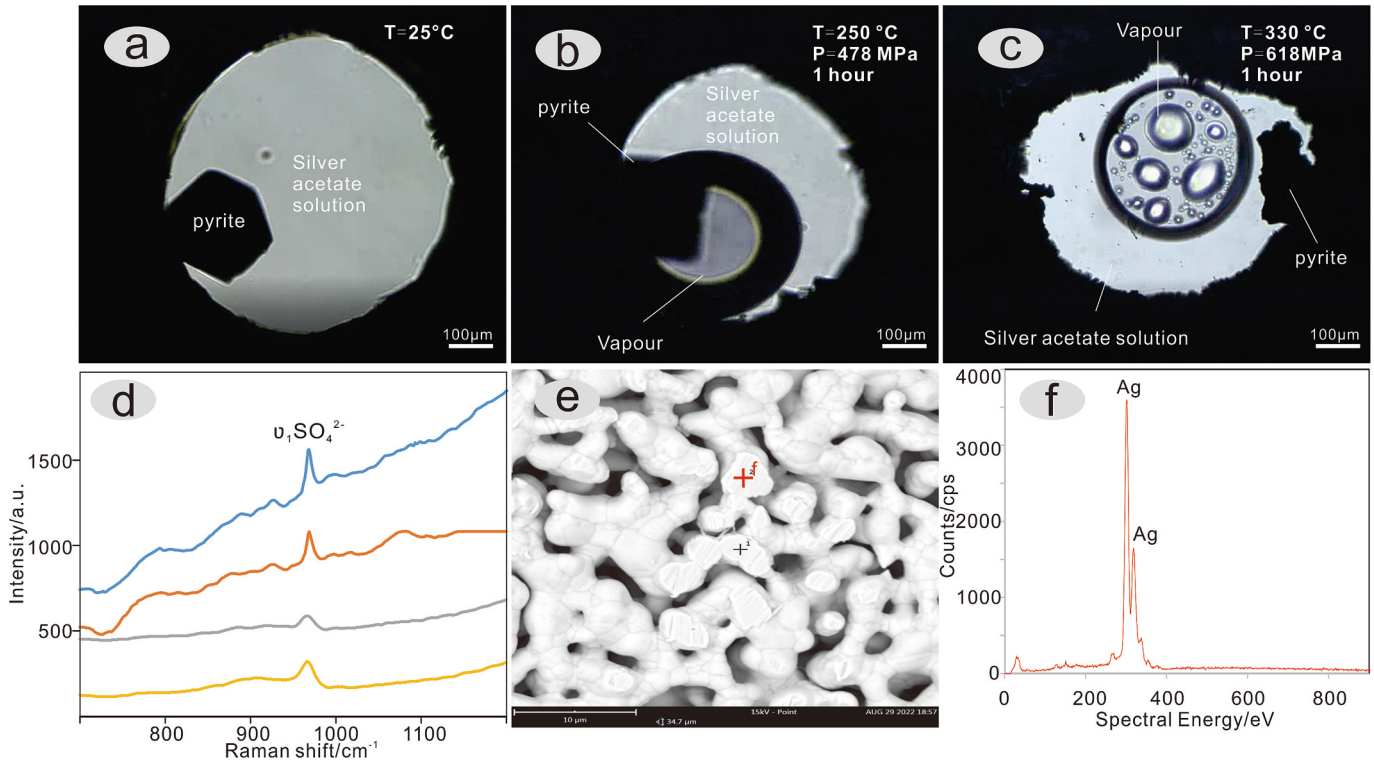

Fig. 5. State of silver acetate solution with pyrite in HDAC at different temperature and pressure. a. Photomicrograph of silver acetate solution with pyrite at the room temperature; b. At the temperature of 250 °C and the pressure of 478 MPa during 1 h, the decomposition of silver acetate solution is characterized by vapour suddenly appearing (photomicrograph); c. Photomicrograph of silver acetate solution at the temperature of 330 °C and the pressure of 618 MPa during 1 h. d. Raman shift of SO_4^{2-}; e. SEM photo of the solid experiment product; f. EDS results show that the solid product is native silver.

ore-forming systems (Yardley, 2005; Zhang et al., 2013). Based on this, silver was added at a concentration of 10 ppm, along with 5 % (by weight) organic carbon to the initial rock. For modeling, we selected the $C_{128}H_{68}O_7$ from the published organic compounds with available thermodynamic data (Ryzhenko et al., 2016). In our model, the initial rock composition was defined at step 0, with pressure and temperature serving as the primary variables along two pathways: T = 50 °C + 3n (where n is the step number, ranging from 1 to 151), resulting in a temperature range of 50 °C to 500 °C; and P = 800 bar + 40n (where n ranges from 1 to 106), resulting in a pressure range of 80 MPa to 500 MPa. The water–rock ratio was set at 1:1, corresponding to 50 kg of carbonaceous shales and an equal amount of water containing 2.5 kg NaCl, representing a low-salinity fluid (5 wt% NaCl). Based on these parameters, P-T pseudosections were generated to quantify the total release of acetate ion (CH_3COO^-), acetic acid (CH_3COOH), CH_3COOAg (aq), $Ag(CH_3COO)_2^-$, CO_2 and CH_4 at each P-T step.

The results of thermodynamic simulations show that the highest concentrations of CH_3COO^- reach approximately 23.6 ppm under conditions of 400 °C and 200–300 MPa. In comparison, the concentrations of CH_3COOH are lower (<1 ppm), but both CH_3COO^- and CH_3COOH concentrations increase with rising temperature and pressure. The lowest concentrations of $CH3COO^-$ and CH_3COOH occur in the regions of high temperature-low pressure and low temperature-high pressure (Fig. 6a, b). Silver-organic complexes, such as CH_3COOAg (aq) and $Ag(CH_3COO)_2^-$, exhibit similar behavior. Below 400 °C, their concentrations are very limited. However, above 400 °C, the concentrations of these silver-organic complexes increase significantly and correlate with rising temperature and pressure (Fig. 6c, d). Moreover, their concentrations are higher at elevated pressure for the same temperature. Carbon dioxide and methane, the most commonly detected inorganic carbon species in fluid inclusions of sediment-hosted silver deposits, are also present in our model. Their distribution patterns differ markedly, as

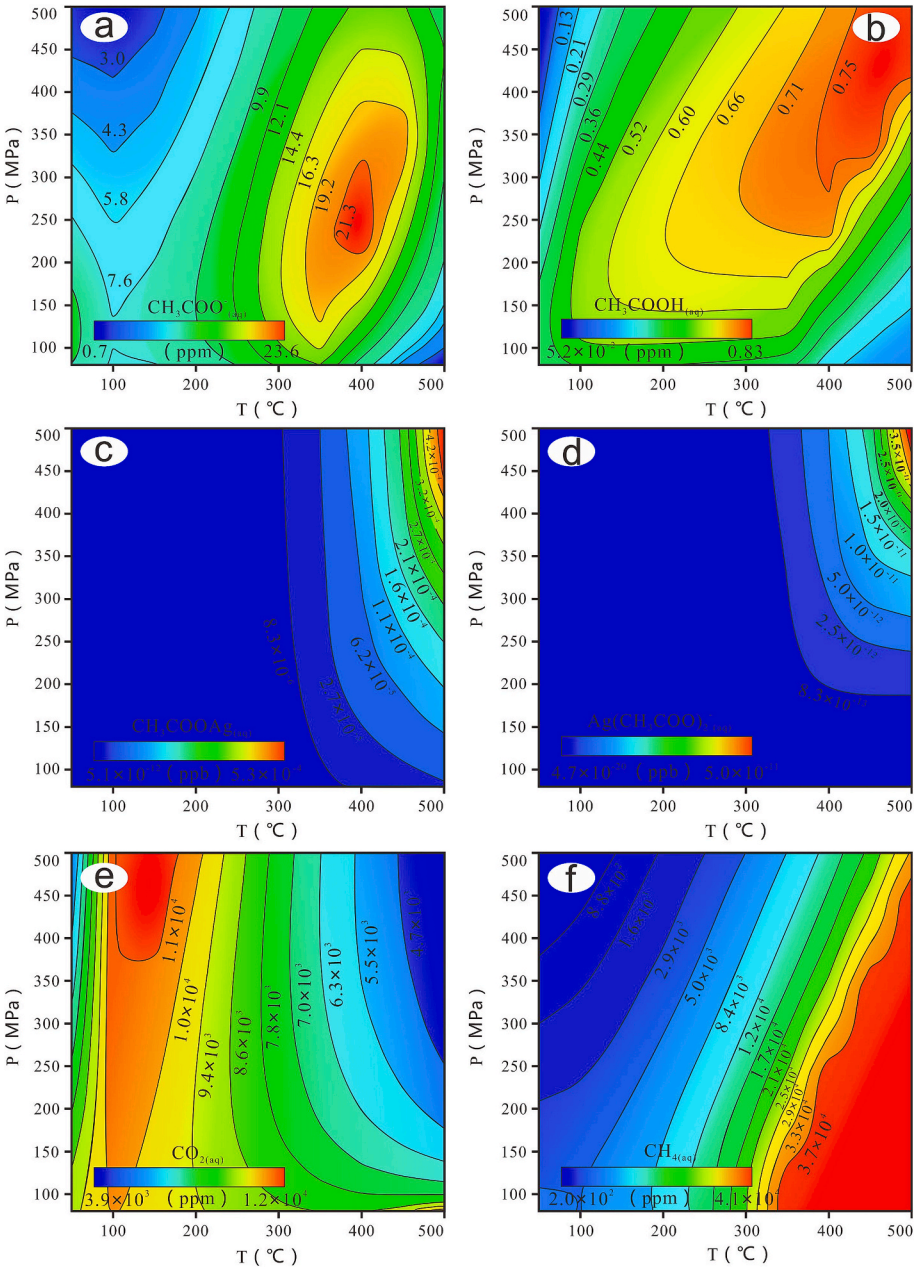

Fig. 6. Contours of carbonic species concentration: (a-b) Contours of e CH_3 COO^- and CH_3 COOH concentration as a proportion of H_2 O; (c-d) Contours of CH_3 COOAg (aq) and $Ag(CH3COO)_2^-$ concentration as a proportion of H_2 O; (e-f) Contours of CO_2 and CH_4 concentration as a proportion of H_2 O.

shown in Fig. 6e, f. The concentrations of CH_4 increase with rising temperature and decreasing pressure, becoming significantly higher above 300 °C. In contrast, the concentrations of CO_2 exhibit a more complex behavior. Their peaking concentrations occur between 100–200 °C, and at temperatures above 200 °C, their concentrations decrease significantly with rising temperature and decreasing pressure.

5. Discussion

5.1. Silver acetate solution is efficient ore-forming fluid

The experiments show that silver acetate is persistent over a wide range of pressures and temperatures, and its decomposition temperatures increase with increasing pressure (Fig. 7). At high pressure (600 MPa), silver acetate could exist at temperature of 300 °C, which is higher than the previously-inferred maximum temperature (200 °C) to keep acetic acid stably exist in large quantities (Giordano, 1994). As shown in Fig. 3, acetate solution can transport silver and other metals upward to the shallow crustal levels under low geothermal gradients (e.g., 25 °C/km), and the metallic acetates tend to decompose under high geothermal gradients (e.g., 50 °C/km; Fig. 7). In other words, the acetate solution prefers to uptake metals from host-rocks and transport metals upward to shallow crustal levels in *syn*-orogenic compression regime, and then discharge transported metals at favorable loci to form ore deposits in post-orogenic thermal extension setting. This understanding accords with the facts that organic acids and CO_2 were commonly observed in sediment-hosted hydrothermal systems (Sanz-Robinson and Williams-Jones, 2019; Tu, 1998), and that the ore metals or minerals of the orogenic-type Au, Ag, Cu and Pb-Zn deposits generally precipitated in the middle mineralization stage under decompression settings (Zhong et al., 2013; Chen et al., 2022 and references therein). Furthermore, the results of thermodynamic simulation that the elevated concentrations of silver acetate in high pressure support our experiment findings. A small amount of silver acetate might exist at more elevated temperature (500 °C) at high pressure (500 MPa). The higher concentrations of acetic acid at conditions of 500 °C and 500 MPa illustrate that acetic acid could be thermodynamically stable under low geothermal gradient, which is also consistent with our experiment results (Equation (1). There are abundant organic acids in oilfield brine. Once formed, silver acetate can be transported to the deep crust or even the mantle with the subduction slab in the orogenic belts. Therefore, silver acetate can not only become an effective ore-forming fluid, but also may participate in the deep carbon cycle process (Sverjensky et al., 2014; Huang et al., 2017).

5.2. The role and source of CO_2 in the hydrothermal mineralization

The experimental results indicate that acetates are vibrant to transport metals under low geothermal gradients, e.g., 15 °C/km (Fig. 3), which corresponds to some subduction zones. Metamorphic devolatilization of the subduction-related oceanic or continental slabs has been considered as the realistic source of the fluids forming orogenic-type deposits (Groves et al., 2020). The subducted sediments usually contain organic matter (Chen et al., 2001; Evans and Tomkins, 2020; Goldfarb et al., 2023), and can generate CO_2 and acetate-bearing fluids capable of transporting metals under low geothermal gradients. Once upward to the shallow crustal levels, particularly, the ductile-to-brittle transition levels, decompression can lead to decomposition of acetate, resulting in CO_2 release and metal precipitation (equation 1 or 2), which helps understanding the widespread occurrence of CO_2-rich inclusions in orogenic-type deposits (Chen et al., 2004; Goldfarb et al., 2005; Pirajno, 2009).

The presence of CO_2 in the fluids hinders decomposition of CH_3COOAg, and keeps metals dissolved in solution, and is helpful for metallic transportation as organic acid compound (Heinrich, 2007; Liebscher, 2007; Chen et al., 2022). The CO_2 presence can also maintain the fluids weakly acidic ($pH < 7$), and keep metallic acetate and/or sulfhydryl complex being stable and transportable in the fluids (Phillips and Evans, 2004). On the contrary, the wall-rock carbonation, which has been generally observed in orogenic-type deposits, will consume CO_2 in solution, and consequently, facilitates metallic acetate decomposition and metal precipitation.

In our experimental processes, no CH_4 was detected, which can be explained by the results of our thermodynamic simulation. It can be seen that the field for CH_4 predominance is above 300 °C, while CO_2 is

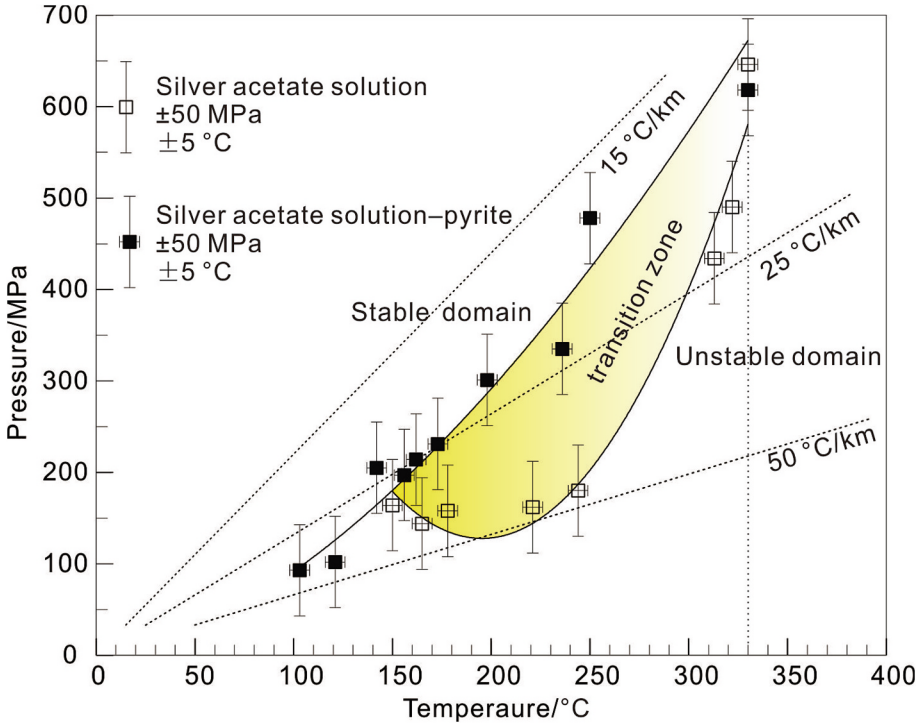

Fig. 7. The stability curves of silver acetate solution system and silver acetate solution with pyrite system (1 h of reaction time).

predominant below 300 °C. In our experiments, majority of temperature conditions do not exceed 300 °C, thus only CO_2 was detected during experimental processes. Decarboxylation caused by high temperature may be the main factor of the increased methane concentration. This finding might account for the fact that CO_2 are the most abundant carbonic fluid inclusions in orogenic mineralization systems, while CH_4 are only reported sometimes (Kerrich et al., 2000; Chen et al., 2007; Goldfarb and Pitcairn, 2023).

5.3. Pyrite formation preluding ore-metal precipitation

As pyrite is common in hydrothermal mineral deposits, particularly in the early and middle mineralization stages of the orogenic-type deposits, it is in need to investigate the impact of pyrite on the persistence and decomposition of metal acetates. In the presence of pyrite, silver acetate decomposes at temperatures of 150 to 330 °C, under geothermal gradient of 25 °C/km (Fig. 7). It can be envisaged that silver acetate solution remains persistent before pyrite precipitation, and the pyrite appearance in early mineralization stage promotes the decomposition of silver acetate and rapid discharges of the metals being transported in the complexation with acetate in middle stage. This understanding accords well with the case of the Weishancheng Au-Ag ore belt in central China, which is formed in an extensional tectonic setting and is characteristic by CO_2-rich ore-forming fluid, carbonaceous-rich orebody and pyrite-bearing quartz vein of early ore-forming stage (Zhang et al., 2013).

6. Conclusion

The role of organic matters might be overlooked in conventional metal mineralization models. We suggest that silver acetate can exist stably at a temperature lower than 300℃, and its decomposition temperature increases with the increase of pressure. These organic matters can bind with silver to form silver acetate transporting silver as potentially ore-forming fluids under lower geothermal gradients. The decomposition of silver acetate was promoted by the increase of temperature, the decrease of pressure, the increase of pH value and the precipitation of pyrite. CO_2 as one of the decomposition products might serve as a buffer to maintain metallic transportation or precipitation. The common observation of carbonate, sericite and quartz alterations, CO_2-rich fluid inclusions and pyrite-bearing quartz vein of early ore-forming stage in hydrothermal deposits, such as orogenic-type lodes, corresponds well with the experimental results of stability and thermal dissociation of silver acetate solution.

Declaration of competing interest

The authors declare that they have no known competing financial interests or personal relationships that could have appeared to influence the work reported in this paper.

Acknowledgments

This work was supported by National Natural Science Foundation of China (Grant Nos. 42273069, U1803242 and U2244206) and the National Deep Resource Planning Project (2017YFC0601203).

Data availability

The data that has been used is confidential.

References

Anderson, G.M., 2008. The mixing hypothesis and the origin of Mississippi Valley-type ore deposits. Econ. Geol. 103, 1683–1690.
Anderson, G.M., 2015. Kerogen as a source of sulfur in MVT deposits. Econ. Geol. 110, 837–840.
Baker, W.E., 1978. The role of humic acid in the transport of gold. Geochim. Cosmochim. Acta 42, 645–649.
Bassett, W.A., Shen, A.H., Bucknum, M., Chou, I.M., 1993. A new diamond anvil cell for hydrothermal studies to 10 GPa and from 190 °C to 1100 °C. Rev. Sci. Instrum. 64, 2340–2345.
Bell, J.L.S., Palmer, D.A., Barnes, H.L., Drummond, S.E., 1994. Thermal decomposition ofacetate: III. Catalysis by mineral surfaces. Geochim. Cosmochim. Acta 58, 4155–4177.
Boles, J.S., Crerar, D.A., Grissom, G., Key, T., 1988. Aqueous thermal degradation of gallic acid. Geochim. Cosmochim. Acta 52, 341–344.
Broadbent, G.C., Myers, R.E., Wright, J.V., 1998. Geology and origin of shale-hosted Zn-Pb-Ag mineralization at the Century Deposit, Northwest Queensland, Australia. Econ. Geol. 90, 1264–1294.
Brown, P.E., Lamb, W.M., 1989. PVT properties of fluids in the system H_2O±CO_2±NaCl: New graphical presentations and implications for fluid inclusion studies. Geochim. Cosmochim. Acta 53, 1209–1221.
Chen, Y.J., Pirajno, F., Li, N., Deng, X.H., and Yang, Y.F., 2022. Geology and geochemistry of molybdenum deposits in the Qinling Orogen, P R China. Springer, Singapore.
Chen, Y.J., Zhang, J., Liu, C.Q., He, S.H., 2001. The lateral source of the continental oil and gas of China: extension and application of the CPMF model. Geol. Rev. 47, 261–271 in Chinese with English abstract.
Chen, Y.J., Pirajno, F., Sui, Y.H., 2004. Isotope geochemistry of the Tieluping silver deposit, Henan, China: a case study of orogenic silver deposits and related tectonic setting. Miner. Deposita 44, 560–575.
Chen, Y.J., Ni, P., Fan, H.R., Pirajno, F., Lai, Y., Su, W.C., Zhang, H., 2007. Diagnostic fluid inclusions of different types hydrothermal gold deposits. Acta Petrol. Sin. 23 (9), 2085–2108 in Chinese with English abstract.
Chou, I.M., Song, Y., Burruss, R.J., 2008. A new method for synthesizing fluid inclusions in fused silica capillaries containing organic and inorganic material. Geochim. Cosmochim. Acta 72, 5217–5231.
Chu, B.L., Shan, Z.H., Wang, G., 2000. Discussion on the characteristics and genesis of Yindongpo gold deposit, Henan. Gold. Geology 6 (1), 33–37 in Chinese with English abstract.
Cui, H., Zhong, R.C., Xie, Y.H., Yuan, X.Y., Liu, W.H., Brugger, J., Yu, C., 2020. Forming sulfate- and REE-rich fluids in the presence of quartz. Geology 48, 145–148.
Ding, Z.P., Sun, X.M., Xu, X.B., Ling, S.M., Xie, Z.R., 2024. Likely gold transportation via organic complexes in sediment-hosted orogenic gold deposits in southern Tibet: From the perspective of thermodynamic modelling. J. Asian Earth Sci. 264, 106068.
Drummond, S.E., Palmer, D.A., 1986. Thermal decarboxylation of acetate. Part II. Boundary conditions for the role of acetate in the primary migration of natural gas and the transportation of metals in hydrothermal systems. Geochim. Cosmochim. Acta 50, 825–833.
Etminan, H., Hoffmann, C.F., 1989. Biomarkers in fluid inclusions: A new tool in constraining source regimes and its implications for the genesis of Mississippi Valley-type deposits. Geology 17, 19–22.
Evans, K.A., Tomkins, A.G., 2020. Metamorphic fluids in orogenic settings. Elements 16, 381–387.
Fein, J.B., Gore, N., Marshall, D., Yassa, L., Loch, A., Brantley, S.L., 1995. The effect of aqueous complexation and gibbsite surface sites on the decarboxylation rate of malonate. Geochim. Cosmochim. Acta 59, 5071–5080.
Fisher, J.B., 1987. Distribution and occurrence of aliphatic acid anions in deep subsurface water. Geochim. Cosmochim. Acta 51, 2459–2468.
Giordano, T.H., 1994. Metal transport in ore fluids by organic ligand complexation. In: Pittman, E.D., Lewan, M.D. (Eds.), Organic Acids in Geological Processes. Berlin, Springer, Heidelberg, pp. 270–319.
Goldfarb, R.J., Pitcairn, I., 2023. Orogenic gold: is a genetic association with magmatism realistic? Miner. Deposita 58, 5–35.
Goldfarb, R.J., Baker, T., Dube, B., Groves, D.I., Hart, C.J.R., Gosselin, P., 2005. Distribution, character and genesis of gold deposits in metamorphic terranes. Econ. Geol. 100, 407–450.
Groves, D.I., Santosh, M., Deng, J., Wang, Q., Yang, L., Zhang, L., 2020. A holistic model for the origin of orogenic gold deposits and its implications for exploration. Miner. Deposita 55, 275–292.
He, R.T., Hu, B.Y., Zhong, H., Jin, F.M., Fan, J.J., Hu, Y.H., Jing, Z.Z., 2019. Reduction of CO_2 with H_2S in a simulated deep-sea hydrothermal vent system. Chem. Commun. 55, 1056–1059.
Heinrich, C.A., 2007. Fluid-fluid interactions in magmatic-hydrothermal ore formation. Rev. Mineral. Geochem. 65, 363–387.
Helgeson, H.C., 1992. Calculation of the thermodynamic properties and relative stabilities of aqueous acetic and chloroacetic acids, acetate and chloroacetates, and acetyl and chloroacetyl chlorides at high and low temperatures and pressures. Appl. Geochem. 7, 291–308.
Holloway, J.R., 1981. Compositions and volumes of supercritical fluids, in Hollister, L.S., and Crawford, M.L., eds., Mineralogical Association of Canada Short Course in Fluid Inclusions, 6, 3−38.
Horita, J., Berndt, M.E., 1999. Abiogenic methane formation and isotopic fractionation under hydrothermal conditions. Science 285, 1055–1057.
Huang, F., Daniel, I., Cardon, H., Montagnac, G., Sverjensky, D.A., 2017. Immiscible hydrocarbon fluids in the deepcarbon cycle. Nat. Commun. 8, 15798.
Jaraula, C.M.B., Schwark, L., Moreau, X., Pickel, W., Bagas, L., Grice, K., 2015. Radiolytic alteration of biopolymers in the Mulga Rock (Australia) uranium deposit. Appl. Geochem. 52, 97–108.
Jin, F.M., Gao, Y., Jin, Y.L., Cao, J.L., Wei, Z., Smith Jr, R.L., 2011. High-yield reduction of carbon dioxide into formic acid by zero-valent metal/metal oxide redox cycles. Energ. Environ. Sci. 4, 881–884.

Jin, F.M., Zeng, X., Jing, Z.Z., Enomoto, H., 2012. A potentially useful technology by mimicking nature—rapid conversion of biomass and CO_2 into chemicals and fuels under hydrothermal conditions. Ind. Eng. Chem. Res. 51, 9921–9937.
Kerrich, R., Goldfarb, R.J., Groves, D., Garwin, S., Jia, Y.F., 2000. The characteristics, origins, and geodynamic settings of supergiant gold metallogenic provinces. Sci. China Ser. D Earth Sci. 43, 1–68.
Kesler, S., Jones, H., Furman, F., Sassen, R., Anderson, W., Kyle, J., 1994. Role of crude oil in the genesis of Mississippi Valley-type deposits: Evidence from the Cincinnati arch. Geology 22, 609–612.
Kharaka, Y.K., Maest, A.S., Carothers, W.W., Law, L.M., Lamothe, P.J., Fries, T.L., 1987. Geochemistry of metal-rich brines from central Mississipi salt dome basin, USA. Appl. Geochem. 2, 543–561.
Liebscher, A., 2007. Experimental studies in model fluid systems. Rev. Mineral. Geochem. 65, 15–47.
Michiels, K., Peeraer, B., Van Dun, W., Spooren, J., Meynen, V., 2015. Hydrothermal conversion of carbon dioxide into formate with the aid of zerovalent iron: the potential of a two-step approach. Faraday Discuss. 183, 177–195.
Mossman, D.J., 1999. Carbonaceous substances in mineral deposits: implications for geochemical exploration. J. Geochem. Explor. 66, 241–247.
Nakano, M., Fujiwara, T., Koga, N., 2016. Thermal decomposition of silver acetate: physico-geometrical kinetic features and formation of silver nanoparticles. J. Phys. Chem. C 120, 8841–8854.
Ni, Z.Y., Chen, Y.J., Zheng, H.F., Li, N., Li, H.P., 2020. Stability of copper acetate at high P-T and the role of organic acids and CO_2 in metallic mineralization. Sci. Rep. 10, 5387.
Palmer, D.A., Drummond, S.E., 1986. Thermal decarboxylation of acetate. Part I. The kinetics and mechanism of reaction in aqueous solution. Geochim. Cosmochim. Acta 50, 813–823.
Phillips, G.N., Evans, K.A., 2004. Role of CO_2 in the formation of gold deposits. Nature 429, 860–863.
Pirajno, F., 2009. Hydrothermal Processes and Mineral Systems. Springer, Berlin.
Reith, F., McPhail, D.C., 2006. Effect of resident microbiota on the solubilization of gold in soil from the Tomakin Park Gold Mine, New South Wales, Australia. Geochim. Cosmoch. Acta 70, 1421–1438.
Ryzhenko, B.N., Sidkina, E.S., Cherkasova, E.V., 2016. Computer simulation of the transformation of natural living matter into kerogen. Geochem. Int. 54, 706–711.
Sanz-Robinson, J., Williams-Jones, A.E., 2019. Zinc solubility, speciation and deposition: A role for liquid hydrocarbons as ore fluids for Mississippi Valley type Zn-Pb deposits. Chem. Geol. 520, 60–68.
Schmidt, C., Ziemann, M.A., 2000. In-situ Raman spectroscopy of quartz: A pressure sensor for hydrothermal diamond-anvil cell experiments at elevated temperatures. Am. Mineral. 85, 1725–1734.
Shock, E.L., 1995. Organic acid in hydrothermal solutions:standard molal thermodynamic properties of carboxylic acids and estimates of dissociation constants at high temperatures and pressures. Am. J. Sci. 295, 496–580.
Shock, E.L., Koretsky, C.M., 1993. Metal-organic complexes in geochemical processes: Calculation of standard partial molal thermodynamic properties of aqueous acetate complexes at high pressures and temperatures. Geochim. Cosmochim. Acta 57, 4899–4922.
Shvarov, Y.V., 2008. HCh: New potentialities for the thermodynamic simulation of geochemical systems offered by windows. Geochem. Int. 46 (8), 834–839.
Sun, Q., 1998. Carboxylate composition of fluid inclusion leachate in the Linglong gold deposit, Shandong Province. Geochemistry 27, 579–584.
Sun, Y.Z., Püttmann, W., 2000. The role of organic matter during copper enrichment in Kupferschiefer from the Sangerhausen basin, Germany. Org Geochem. 31, 1143–1161.
Sverjensky, D.A., Shock, E.L., Helgeson, H.C., 1997. Prediction of the thermodynamic properties of aqueous metal complexes to 1000°C and 5 kb. Geochim. Cosmochim. Acta 61, 1359–1412.
Sverjensky, D.A., Stagno, V., Huang, F., 2014. Important role for organic carbon in subduction-zone fluids in the deep carbon cycle. Nat. Geosci. 7, 909–913.
Tissot, B.P., Welte, D.H., 2013. Petroleum Formation and Occurrence. Springer, Berlin.
Tu, G.Z., 1998. Low-Temperature Geochemistry. Science Press, Beijing in Chinese.
Yardley, B.W.D., 2005. Metal concentrations in crustal fluids and their relationship to ore formation. Econ. Geol. 100, 613–632.
Yuan, X.Y., Mayanovic, R.A., Zheng, H.F., 2016. Determination of pressure from measured Raman frequency shifts of anhydrite and its application in fluid inclusions and HDAC experiments. Geochim. Cosmochim. Acta 194, 253–265.
Zhang, J., Chen, Y.J., Pirajno, F., Deng, J., Chen, H.Y., Wang, C.M., 2013. Geology, C-H-O-S-Pb isotope systematics and geochronology of the Yindongpo gold deposit Tongbai Mountains, central China: implication for ore genesis. Ore Geol. Rev. 53, 343–356.
Zhong, R.C., Li, W.B., Chen, Y.J., Yue, D.C., Yang, Y.F., 2013. P-T-X conditions, origin, and evolution of Cu-bearing fluids of the shear zone-hosted Huogeqi Cu–(Pb–Zn–Fe) deposit, northern China. Ore Geol. Rev. 50, 83–97.
Zhong, R.C., Brugger, J., Tomkins, A.G., Chen, Y.J., Li, W.B., 2015. Fate of gold and base metals during metamorphic devolatilization of a pelite. Geochim. Cosmochim. Acta 171, 338–352.
Zhong, H., Yao, G.D., Cui, X., Yan, P., Wang, X.G., Jin, F.M., 2019. Selective conversion of carbon dioxide into methane with a 98% yield on an in situ formed Ni nanoparticle catalyst in water. Chem. Eng. J. 357, 421–427.